DTU Library

The 0.3-30 Kev Spectra Of Powerful Starburst Galaxies: Nustar And Chandra Observations Of Ngc 3256 And Ngc 3310

Lehmer, B. D.; Tyler, J. B.; Hornschemeier, A. E.; Wik, D. R.; Yukita, M.; Antoniou, V.; Boggs, S.; Christensen, Finn Erland; Craig, W. W.; Hailey, C. J.

THE 0.3–30 keV SPECTRA OF POWERFUL STARBURST GALAXIES: *NuSTAR* AND *CHANDRA* OBSERVATIONS OF NGC 3256 AND NGC 3310

B. D. Lehmer[1,2], J. B. Tyler[2,3], A. E. Hornschemeier[2], D. R. Wik[1,2], M. Yukita[1,2], V. Antoniou[4], S. Boggs[5], F. E. Christensen[6], W. W. Craig[5,7], C. J. Hailey[8], F. A. Harrison[9], T. J. Maccarone[10], A. Ptak[2], D. Stern[11], A. Zezas[4,12,13], AND W. W. Zhang[2]

[1] The Johns Hopkins University, Homewood Campus, Baltimore, MD 21218, USA
[2] NASA Goddard Space Flight Center, Code 662, Greenbelt, MD 20771, USA
[3] Institute for Astrophysics and Computational Sciences, Department of Physics, The Catholic University of America, Washington, DC 20064, USA
[4] Harvard-Smithsonian Center for Astrophysics, 60 Garden Street, Cambridge, MA 02138, USA
[5] Space Sciences Laboratory, University of California, Berkeley, CA 94720, USA
[6] DTU Space-National Space Institute, Technical University of Denmark, Elektrovej 327, DK-2800 Lyngby, Denmark
[7] Lawrence Livermore National Laboratory, Livermore, CA 94720, USA
[8] Columbia Astrophysics Laboratory, Columbia University, New York, NY 10027, USA
[9] Caltech Division of Physics, Mathematics and Astronomy, Pasadena, USA
[10] Department of Physics, Texas Tech University, Lubbock, TX 79409, USA
[11] Jet Propulsion Laboratory, California Institute of Technology, Pasadena, CA 91109, USA
[12] Physics Department & Institute of Theoretical & Computational Physics, University of Crete, 71003 Heraklion, Crete, Greece
[13] Foundation for Research and Technology-Hellas, 71110 Heraklion, Crete, Greece

ABSTRACT

We present nearly simultaneous *Chandra* and *NuSTAR* observations of two actively star-forming galaxies within 50 Mpc: NGC 3256 and NGC 3310. Both galaxies are significantly detected by both *Chandra* and *NuSTAR*, which together provide the first-ever spectra of these two galaxies spanning 0.3–30 keV. The X-ray emission from both galaxies is spatially resolved by *Chandra*; we find that hot gas dominates the $E < 1$–3 keV emission while ultraluminous X-ray sources (ULXs) provide majority contributions to the emission at $E > 1$–3 keV. The *NuSTAR* galaxy-wide spectra of both galaxies follow steep power-law distributions with $\Gamma \approx 2.6$ at $E > 5$–7 keV. Using new and archival *Chandra* data, we search for signatures of heavily obscured or low luminosity active galactic nuclei (AGNs). We find that both NGC 3256 and NGC 3310 have X-ray detected sources coincident with nuclear regions; however, the steep *NuSTAR* spectra of both galaxies restricts these sources to be either low luminosity AGNs ($L_{2-10\,\rm keV}/L_{\rm Edd} \lesssim 10^{-5}$) or non-AGNs in nature (e.g., ULXs or crowded X-ray sources that reach $L_{2-10\,\rm keV} \sim 10^{40}$ erg s^{-1} cannot be ruled out). Combining our constraints on the 0.3–30 keV spectra of NGC 3256 and NGC 3310 with equivalent measurements for nearby star-forming galaxies M83 and NGC 253, we analyze the star formation rate (SFR) normalized spectra of these starburst galaxies. The spectra of all four galaxies show sharply declining power-law slopes at energies above 3–6 keV primarily due to ULX populations. Our observations therefore constrain the average spectral shape of galaxy-wide populations of luminous accreting binaries (i.e., ULXs). Interestingly, despite a completely different galaxy sample selection, emphasizing here a range of SFRs and stellar masses, these properties are similar to those of super-Eddington accreting ULXs that have been studied individually in a targeted *NuSTAR* ULX program. We also find that NGC 3310 exhibits a factor of $\approx$3–10 elevation of X-ray emission over the other star-forming galaxies due to a corresponding overabundance of ULXs. We argue that the excess of ULXs in NGC 3310 is most likely explained by the relatively low metallicity of the young stellar population in this galaxy, a property that is expected to produce an excess of luminous X-ray binaries for a given SFR.

Key words: galaxies: active – galaxies: individual (NGC 3256 and NGC 3310) – galaxies: starburst – galaxies: star formation – X-rays: galaxies

1. INTRODUCTION

With the launch of the *NuSTAR* X-ray observatory (Harrison et al. 2013), we now have the first-ever means for studying populations of normal galaxies (not hosting luminous active galactic nuclei (AGNs)) in the $\approx$10–30 keV bandpass, an energy regime which is expected to be dominated by bright X-ray binaries and low-level contributions from diffuse inverse-Compton emission (e.g., Persic & Rephaeli 2002; Wik et al. 2014a). The spectra of X-ray binaries at these energies betray unique information about their accretion states as variations in accretion disk, reflection, and coronal components undergo strong spectral pivots above $\approx$10 keV (see, e.g., Done et al. 2007), a regime that was not previously probed by *Chandra* and *XMM-Newton* for sources outside the Local Group. Prior to *NuSTAR*, studies of the hard X-ray spectra of X-ray binaries was limited to objects in the Milky Way (MW) and Magellanic Clouds (e.g., via *RXTE*; see Remillard & McClintock 2006 for a review), providing limited information about how the accretion states of these populations vary with galaxy properties (e.g., the starburst environment).

With *Chandra* and *XMM-Newton*, the lower-energy <10 keV emission from local galaxies has been studied in detail for a variety of galaxy types (see, e.g., Fabbiano et al. 2006 for a review), and ultradeep *Chandra* observations have extended these studies to very distant galaxy populations with look-back times that span the vast majority of cosmic history (e.g., Basu-Zych et al. 2013a). We are detecting X-ray emission from
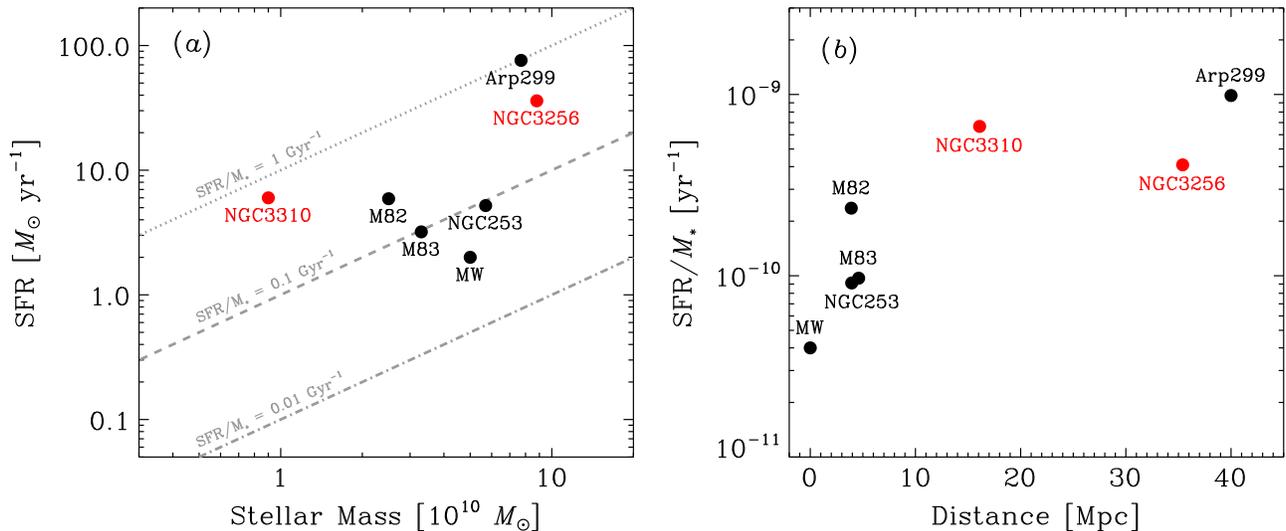
Figure 1. Physical properties of *NuSTAR* starburst galaxies sample. (a) SFR vs. $M_\star$ for the full sample with regions of constant specific SFR (sSFR $\equiv$ SFR/$M_\star$) highlighted. (b) sSFR vs. distance for the full sample. For comparison, the location of the Milky Way (MW) has been indicated. Our sample consists of galaxies with sSFRs that range from being comparable to those of the MW to a factor of ≈ 20 times higher. We therefore expect that the X-ray emitting point-source populations in our sample will be skewed toward including richer populations of HMXBs compared to the MW (e.g., Lehmer et al. 2010; Mineo et al. 2012a). NGC 3256 and NGC 3310 are among the highest sSFR galaxies in our sample.

galaxy populations out to $z \approx 4$ where the observed-frame *Chandra* 0.5–8 keV band corresponds to rest-frame energies of 2.5–40 keV, the most sensitive regimes of the *NuSTAR* bandpass for extragalactic binary work. Results from such studies have prompted the development of accreting binary population synthesis models, which have successfully been employed to construct a self-consistent framework that describes the observed evolution of X-ray binary populations from cosmic dawn to today (e.g., Fragos et al. 2013a, 2013b). Key to these observational interpretations and model predictions, however, is knowledge of the X-ray spectra at $\gtrsim 10$ keV for galaxy populations that cover a broad range of physical properties (e.g., Fragos et al. 2013a; Kaaret et al. 2014). Therefore, a next step to improving our understanding of X-ray binary populations is to constrain the distributions and duty cycles of their accretion states and measure how their resulting $\gtrsim 10$ keV spectral contributions vary with galaxy physical properties (e.g., star formation rate (SFR) and stellar mass ($M_\star$)).

We are conducting a joint *NuSTAR* and *Chandra* survey of six far-infrared bright starburst galaxies (NGC 253, M82, M83, Arp 299, NGC 3256, and NGC 3310) with the goal of quantifying the dominant processes that contribute to the $\gtrsim 10$ keV emission. Figure 1 displays the SFR versus $M_\star$ and specific SFR (sSFR $\equiv$ SFR/$M_\star$) versus distance planes for the full galaxy sample. Our key goals are to: (1) identify the accretion states of the most luminous X-ray binary populations in these galaxies and characterize the ≈ 0.3–30 keV spectral energy distributions (SEDs) as a function of the galaxy physical properties (e.g., SFR and $M_\star$); (2) search for heavily obscured AGN that may be present in these actively star-forming galaxies; and (3) constrain the nature of inverse Compton emission associated with particle accelerations in starburst flows.

As a pilot program, we studied with *NuSTAR* and *Chandra* the nuclear region and galaxy-wide X-ray emission of the nearby starburst galaxy NGC 253 (Lehmer et al. 2013; Wik et al. 2014a). These studies showed that there was no

evidence for powerful buried AGN activity in the nucleus, and that the galaxy-wide X-ray emission above 10 keV is dominated by a few ultraluminous X-ray sources (ULXs) with minority contributions from lower luminosity X-ray binaries that have *NuSTAR* colors similar to Galactic black hole binaries in intermediate accretion states. The galaxy-wide X-ray spectrum of NGC 253 steepens at energies above ≈ 6 keV, consistent with the spectra of other ULXs studied by *NuSTAR* (see, e.g., Bachetti et al. 2013; Walton et al. 2013, 2014; Rana et al. 2014), signaling a possible dominance of super-Eddington accreting objects in the overall starburst galaxy spectra.

More recently, we have executed joint *NuSTAR* and *Chandra*/*XMM-Newton* observations of M83 (M. Yukita et al. 2015, in preparation) and Arp 299 (Ptak et al. 2014), galaxies with sSFRs that are comparable to and ≈ 20 times higher than that of the MW, respectively. The brightest X-ray sources in M83 have *NuSTAR* colors similar to those of NGC 253, albeit with fewer ULXs. Arp 299 has $\gtrsim 10$ keV emission dominated by a single Compton-thick AGN that outshines the other X-ray emitting components of the galaxy. Given the relatively large distance (≈ 40 Mpc) to Arp 299, and its correspondingly smaller angular extent, it was not possible to spatially resolve the X-ray emitting components with *NuSTAR*. Therefore, the spectral properties of the non-AGN components were poorly constrained at energies above ≈ 10 keV, leaving us with little knowledge of the high-energy spectral shape for high sSFR galaxies (see Figure 1(b)).

In this paper, we continue to investigate the 0.3–30 keV SEDs of starburst galaxies by studying two powerful starburst galaxies in the local universe: NGC 3256 and NGC 3310. The sSFRs of these galaxies are the second and third highest of our sample (see Figure 1), and are only exceeded by Arp 299. Both NGC 3256 and NGC 3310 have been studied extensively across the full electromagnetic spectrum, and neither system exhibits compelling evidence for harboring a powerful AGN (see Section 2 for a discussion). The sSFRs of these galaxies are ≈ 0.4–0.8 Gyr^{-1}, a range expected to host X-ray binary

populations that are dominated by high-mass X-ray binaries (HMXBs; e.g., Colbert et al. 2004; Lehmer et al. 2010). Such high-sSFR galaxies are representative of the typical galaxy populations on the "main sequence" at $z \approx 1$–2 (e.g., Karim et al. 2011). As such, this study will provide SED constraints on high-sSFR galaxies that can be used to inform X-ray studies of high-redshift galaxy populations at these redshifts, which require informed K-corrections (e.g., Lehmer et al. 2008; Basu-Zych et al. 2013a; Kaaret 2014).

Throughout this paper, we assume distances of $D = 35.4$ and 19.8 Mpc (Sanders et al. 2003) and column densities of $N_{\rm H} = 9.6 \times 10^{20}$ and 1.1×10^{20} cm^{-2} for NGC 3256 and NGC 3310, respectively (Dickey & Lockman 1990). SFR and stellar masses quoted throughout this paper were calculated assuming a Kroupa (2001) initial mass function. SFR were calculated using Equation (6.11) of Calzetti (2013), making use of UV and mid-IR data from *GALEX* and *Spitzer*, respectively. Stellar masses were estimated following the prescription outlined in Appendix 2 of Bell et al. (2003), making use of $B - V$ colors from RC3 (de Vaucouleurs et al. 1991) and K-band luminosities based on 2MASS photometry (Jarrett et al. 2003) and the adopted distances. These assumptions imply SFR $\approx 36\,M_\odot$ yr^{-1} and $6\,M_\odot$ yr^{-1} and $M_\star \approx 9 \times 10^{10}\,M_\odot$ and $9 \times 10^9\,M_\odot$ for NGC 3256 and NGC 3310, respectively. Quoted errors associated with spectral fits represent 90% confidence intervals.

2. THE GALAXIES

2.1. NGC 3256

NGC 3256 (35.4 Mpc) is a major-merger system composed of two gas-rich galaxies with comparable masses (total $M_\star \approx 10^{11}\,M_\odot$) that are in a nearly coalescent phase of the merger (Lípari et al. 2000; Alonso-Herrero et al. 2002). Two discrete nuclei have been identified ≈ 5 arcsec apart (850 pc; Zenner & Lenzen 1993; Norris & Forbes 1995) and remarkably long (200 kpc) H I tidal features have been identified (e.g., Graham et al. 1984; English et al. 2003). The system has the highest 8–1000 μm infrared luminosity ($L_{\rm IR} \approx 4 \times 10^{11}\,L_\odot$; Sanders et al. 2003) for galaxies that reside within $z \lesssim 0.01$, and studies at radio (e.g., Norris & Forbes 1995), submm (e.g., Sakamoto et al. 2006, 2014), infrared (Graham et al. 1984; Doyon et al. 1994a, 1994b; Moorwood & Oliva 1994; Lira et al. 2008; Alonso-Herrero et al. 2013), optical (e.g., Heckman et al. 2000; Lípari et al. 2000; Alonso-Herrero et al. 2002), and UV (e.g., Kinney et al. 1993; Leitherer et al. 2013) wavelengths all support a scenario in which the majority of the galaxy's power output is produced by starburst-related activity.

X-ray studies with *Chandra* and *XMM-Newton* have shown that the 0.3–10 keV spectrum of NGC 3256 can be modeled well as a multiphase thermal plasma with harder power-law emission from a population of discrete point sources, the majority of which are ULXs (see, e.g., Lira et al. 2002; Jenkins et al. 2004; Pereira-Santaella et al. 2011). Although both nuclear regions have been detected by *Chandra* with $L_{\rm 2-10\,keV} \sim 10^{40}$ erg s^{-1}, the nature of the X-ray emission is unclear, as no obvious AGN signatures have been found (Lira et al. 2002). Detailed assessment of the kinematics of the molecular gas, via ALMA and SMA observations, have concluded that both nuclei contain powerful outflows, but with differing characteristics (e.g., Cicone et al. 2014; Emonts et al. 2014; Sakamoto et al. 2014). The northern nuclear

outflow is of wide breadth and has a mean velocity of a few 100 km s^{-1} and is likely driven by a starburst superwind. The southern outflow is well-collimated and faster ($\gtrsim 1000$ km s^{-1}) and is plausibly driven by an AGN that has recently gone dormant (e.g., Moran et al. 1999; Neff et al. 2003; Alonso-Herrero et al. 2012).

2.2. NGC 3310

NGC 3310 is a closer (19.8 Mpc) starburst system with a SFR that is a factor of ~ 10 times lower than NGC 3256 ($L_{\rm IR} \approx 4 \times 10^{10}\,L_\odot$; Sanders et al. 2003); however, given its relatively low stellar mass ($M_\star \lesssim 10^{10}\,M_\odot$), this system has a comparable and perhaps larger sSFR than NGC 3256 (see Figure 1). The system contains evidence for a minor-merger that has triggered a vigorous, young (≈ 2.5–5 Myr old) circumnuclear star-forming ring with a ≈ 20–30 arcsec (≈ 2 kpc) diameter (e.g., Balick & Heckman 1981; Díaz et al. 2000; Elmegreen et al. 2002; Chandar et al. 2005; Miralles-Caballero et al. 2014). The most recent minor merger was inferred to occur in the last ≈ 30 Myr (Elmegreen et al. 2002; de Grijs et al. 2003a), and is likely to be one of several past interactions with small metal-poor dwarf galaxies (e.g., Wehner et al. 2006), as evidence for starburst activity as old as 100 Myr is apparent in the star clusters (Meurer 2000). Such a series of minor-mergers could potentially provide a significant increase to the mass build-up of the bulge (Miralles-Caballero et al. 2014) and is likely to have modified the gas-phase abundances, as there is evidence that the circumnuclear metallicity is lower than is typical for spiral galaxies with morphologies similar to NGC 3310 (e.g., Pastoriza et al. 1993).

Similar to NGC 3256, the *Chandra* and *XMM-Newton* spectra of NGC 3310 can be modeled well by a multiphase hot gas plus a power-law component; however, the plasma temperature is cooler and the power-law slope is harder than those found for NGC 3256 (Jenkins et al. 2004). The hard power-law component is dominated by a population of ≈ 9 ULXs that are distributed within the circumnuclear star-forming ring and along the spiral arms. *HST* STIS observations of the nuclear region have uncovered a bright ≈ 0.5 arcsec (≈ 40 pc) diameter central star-forming region with kinematic properties consistent with a circularly rotating disk (Pastorini et al. 2007). The nuclear region is detected by *Chandra* as a point-like source,[14] and the luminosity of this region, $L_{\rm 2-10\,keV} \sim 10^{40}$ erg s^{-1}, is within the range of other ULXs in the galaxy. The *Chandra* spectrum shows that the nuclear X-ray source has a flat power-law spectral slope, with some evidence (at the 2σ confidence level) for an Fe Kα line—two properties that indicate there may be a hidden (obscured) AGN in the galaxy nucleus (Tzanavaris et al. 2007).

3. OBSERVATIONS AND DATA REDUCTION

In this investigation we make use of nearly simultaneous observations with *NuSTAR* and *Chandra* to explore the full 0.3–30 keV bandpass properties. In later sections, we make use of archival *Chandra* data to support our analyses; however, we focus the current investigation on the new nearly simultaneous observations. We obtained our *NuSTAR* and *Chandra* observations of NGC 3256 and NGC 3310 over single epochs

---

[14] The nuclear region is also detected by *XMM-Newton*; however, it is clear that confusion with four other *Chandra*-resolved ULXs of comparable brightness makes it difficult to uniquely interpret those data.
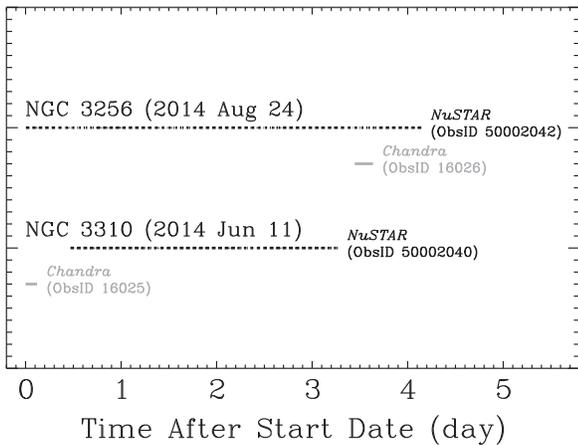
Figure 2. Relative *NuSTAR* (black lines) and *Chandra* (gray lines) observational coverage for NGC 3256 (top) and NGC 3310 (bottom). For clarity, we have annotated the starting date of the observational epoch. The apparently broken up *NuSTAR* observational intervals are due primarily to Earth occultations and passages through the SAA, which result in observing efficiencies of ≈51%–58% on average.

beginning on 2014 August 24 and 2014 June 11, respectively. Figure 2 shows the relative observing schedules for the *NuSTAR* and *Chandra* exposures. Due to Earth occultations and passages through the South Atlantic Anomaly (SAA), the *NuSTAR* on-target observations were carried out at ≈51%–58% efficiency over ≈3–4 days periods. The cumulative *NuSTAR* good-time-interval exposures were 184 ks (ObsID 50002042) and 141 ks (ObsID 50002040) for NGC 3256 and NGC 3310, respectively. The *Chandra* observations were continuous and lasted 16 ks (ObsID 16026) and 10 ks (ObsID 16025) for NGC 3256 and NGC 3310, respectively.

The *NuSTAR* data were reduced using HEASoft v6.15, *NuSTAR* Data Analysis Software (NuSTARDAS) v1.7, and CALDB version 20130320. We processed level 1 data to level 2 products by running nupipeline, which performs a variety of data reduction steps, including (1) filtering out bad pixels, (2) screening for cosmic rays and observational intervals when the background was too high (e.g., during passes through the SAA), and (3) projecting accurately the events to sky coordinates by determining the optical axis position and correcting for the dynamic relative offset of the optics bench to the focal plane bench due to motions of the 10 m mast that connects the two benches.

Due to the angular extents of NGC 3256 and NGC 3310 (major-axes $2a = 3.8$ arcmin and 3.1 arcmin, respectively), the *Chandra* exposures for both galaxies were conducted using single ACIS-S pointings with the approximate position of the galactic centers set as the aimpoints. For our data reduction, we used CIAO v. 4.6 with CALDB v. 4.6.1.1. We reprocessed our events lists, bringing level 1 to level 2 using the script chandra_repro, which identifies and removes events from bad pixels and columns, and filters events lists to include only good time intervals without significant flares and non-cosmic ray events corresponding to the standard *ASCA* grade set (grades 0, 2, 3, 4, 6). We constructed an initial *Chandra* source catalog by searching the 0.5–7 keV images with wavdetect (run with a point-spread function (PSF) map created using mkpsfmap), which was set at a false-positive probability threshold of 2×10^{-5} and run over seven scales from 1–8

(spaced out by factors of $\sqrt{2}$ in wavelet scale: 1, $\sqrt{2}$, 2, $2\sqrt{2}$, 4, $4\sqrt{2}$, and 8). Using these initial *Chandra* source catalogs, we constructed source-free light curves and searched for flaring intervals that were 5σ above the background level. No such intervals were found, and our observations were deemed to be sufficiently cleaned.

In Figure 3, we show the adaptively smoothed, false color *Chandra* images of NGC 3256 and NGC 3310, with *NuSTAR* 4–25 keV intensity contours overlaid. It is apparent from the *Chandra* data that diffuse emission at $E < 1$ keV, potentially due to hot gas and unresolved point sources, and multiple bright point sources at all energies provide dominant contributions to the *Chandra*-detected emission for both galaxies. The *NuSTAR* PSF has an 18 arcsec FWHM core with a 58 arcsec half-power diameter (Harrison et al. 2013). Given the X-ray extents of the galaxies (60–70 arcsec), *NuSTAR* is unable to strictly resolve the point-source populations that dominate the $E > 3$ keV emission probed by *NuSTAR*; however, some evidence for spatial extent following the point-source distribution is apparent in NGC 3310 (see Section 4.3 below).

4. ANALYSIS AND RESULTS

As discussed in Section 1, our primary goals are to measure and assess the contributing components to the broadband 0.3–30 keV SEDs of the two powerful starburst galaxies NGC 3256 and NGC 3310, and constrain the underlying AGN activity in these galaxies. To achieve these goals, we first characterized the 0.3–30 keV spectra across the full extents of both galaxies. We then used the high spatial resolution of *Chandra* to measure the $\lesssim 8$ keV contributions from bright resolved point-sources and diffuse emission from hot gas and unresolved point-sources. Finally, using sensible extrapolations of the *Chandra* component spectra to $\gtrsim 8$ keV, we infer the relative contributions AGN candidates would make to the *NuSTAR* galaxy-wide spectra. In the sections below, we describe each of these procedures in detail.

4.1. Galaxy-wide Spectral Analyses

We began by extracting the nearly simultaneous *Chandra* and *NuSTAR* spectra over the full extents of both galaxies. For NGC 3256 and NGC 3310, we extracted on-source spectra using circular apertures with radii r_{src} equal to 80 and 90 arcsec, respectively. These apertures were chosen to encompass the entire optical extents of the galaxies and reach 20 arcsec (roughly the *NuSTAR* FWHM) beyond the most offset point-sources that were clearly detected with *Chandra*. For each galaxy, background spectra were extracted using 1–5 circular apertures located in source-free regions. For *Chandra*, the background extraction regions had radii ≈50–70 arcsec and were chosen by eye to be placed in a pattern surrounding the on-source extraction region. For *NuSTAR*, background regions were chosen more carefully to properly account for the spatial background gradients that arise primarily from the "aperture" background component, which contains cosmic X-ray background stray light that shines directly onto the detectors from a ≈1°–4° annular region (see, e.g., Appendix A of Wik et al. 2014b). Following the procedure described in Appendix B of Wik et al. (2014b), we constructed background maps for the FPMA and FPMB modules in the 3–20 keV band, an energy regime sensitive to variations in the aperture
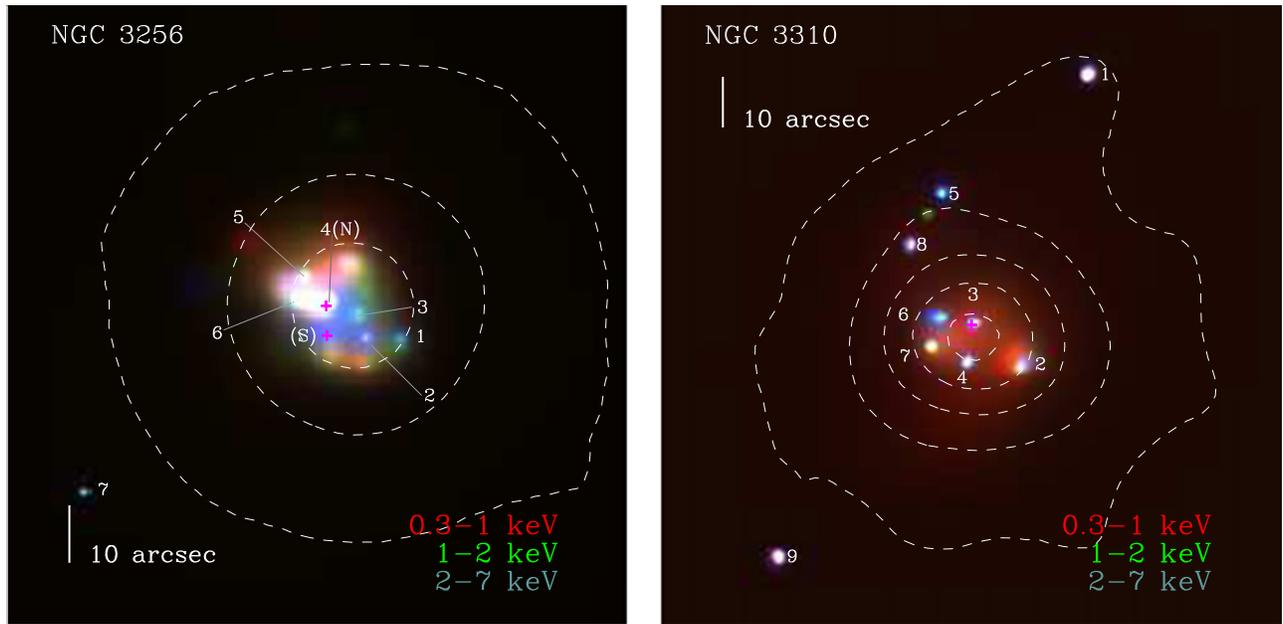
Figure 3. Three-color adaptively smoothed *Chandra* images of NGC 3256 and NGC 3310 with 4–25 keV *NuSTAR* intensity contours overlaid (dashed curves). The three bandpasses, 0.3–1 keV (red), 1–2 keV (green), and 2–7 keV (blue) were chosen to highlight the diffuse components from hot gas and unresolved point sources, as well as absorption in the bright point-source populations. A 10 arcsec bar has been added to each figure for reference. The annotated source numbers, ordered by increasing R.A., highlight bright point sources that are studied in Section 4.3 and presented in Table 2. The locations of galactic nuclei are indicated with magenta crosses. For NGC 3256, the northern (N) and southern (S) nuclei are labeled. With *Chandra*, we detect the northern nucleus of NGC 3256 (source 4, left) and the nuclear region of NGC 3310 (source 3, right). The *NuSTAR* FWHM is ≈18 arcsec, which is sufficient for resolving some structure in the nearer NGC 3310; however, the *NuSTAR* emission for NGC 3256 is consistent with a single source PSF.
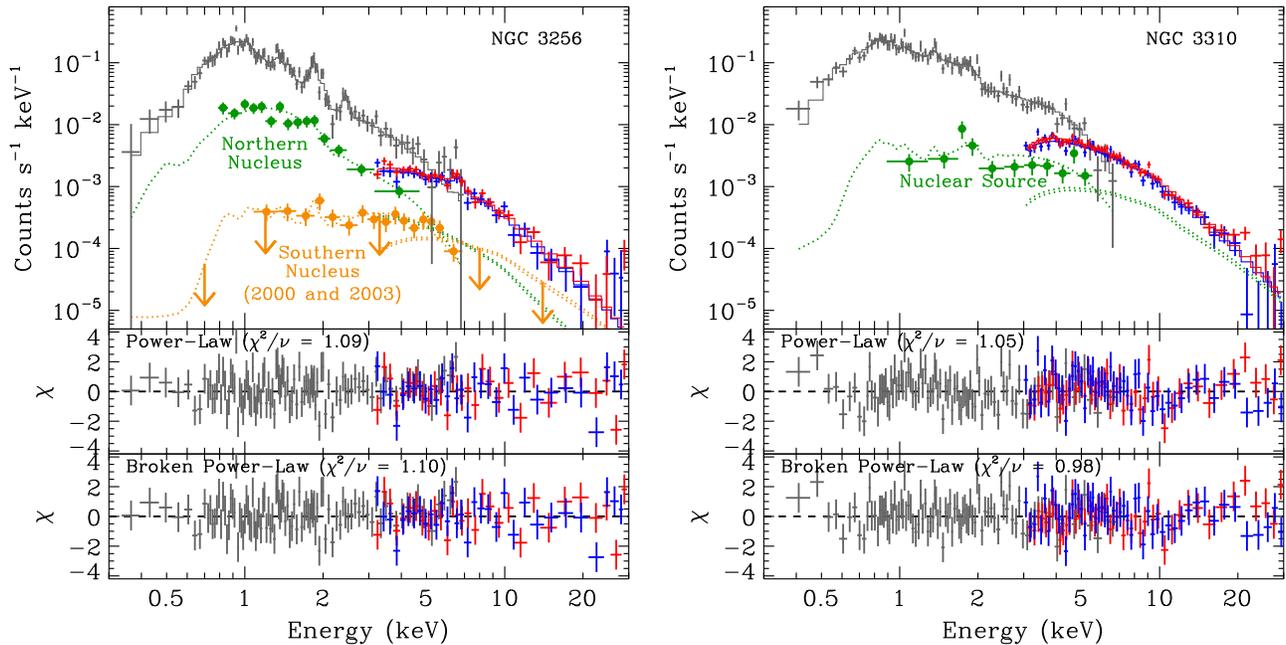

Figure 4. Joint nearly simultaneous *Chandra* (gray) and *NuSTAR* (red for FPMA and blue for FPMB) spectra for the full galactic extents of NGC 3256 (left) and NGC 3310 (right). The diffuse emission that is spatially isolated with *Chandra* was used to constrain two-temperature thermal (apec) models for both galaxies. For NGC 3256, an additional obscured thermal component (≈1 keV) was added to account for hot gas emission associated with the nuclear starburst. Absorbed single and broken power-law models that account for the *Chandra*-detected binaries were both tested for each galaxy, and the resulting residuals are displayed, and goodness-of-fit values are annotated, in the bottom two panels of each plot. We find that a single power-law is sufficient to fit the non-thermal emission from NGC 3256, while a broken power-law is preferred in the case of NGC 3310. We also display the contributions from nuclear components of these galaxies, with extrapolations to the *NuSTAR* band. For NGC 3256, this includes contributions from two nuclear regions associated with two galaxies in the merger: the northern nucleus contribution (green curve) and the estimated upper limit to the southern nucleus contribution (orange curve). The southern nucleus was not formally detected in our 2014 observation, and the upper limit spectrum here indicates the average *Chandra* spectrum from deeper observations in 2000 and 2003 scaled to the upper limit flux of our 2014 observation. We note that the southern nuclear region of NGC 3256 and the nuclear region of NGC 3310 both have flat X-ray spectra and are candidate low luminosity AGN (see Section 4.3 for details).

5

background component. For each background map, we identified 1–4 regions with sizes equal to the on-source aperture that had background levels comparable to those expected to be present within the source extraction regions. The closest edge of each background region was located $>1.2 \times r_{\rm src}$ away from the central positions of each galaxy to avoid contamination from the galaxy itself. After choosing appropriate regions, the *Chandra* and *NuSTAR* on-source and background spectra were extracted using the `specextract` and `nuproducts` tools, respectively.

In Figure 4, we show the 0.3–30 keV galaxy-wide spectra for both galaxies. As discussed in Section 3, from the *Chandra* data (see Figure 3), it is clear that the X-ray emission from both galaxies can be broadly characterized as consisting of diffuse emission (from hot gas and unresolved point sources) and bright point sources (e.g., X-ray binaries and possibly AGNs). Previous investigations with *Chandra* and *XMM-Newton* have found that the diffuse components of these galaxies can be modeled well using two-temperature thermal spectra, with NGC 3310 having cooler temperatures ($kT = 0.3$ and 0.6 keV) than the more powerful NGC 3256 ($kT = 0.6$ and 0.9 keV), which may also contain an additional absorbed hot (≈ 3.9 keV) component (e.g., Lira et al. 2002; Jenkins et al. 2004). The brightest point sources in these galaxies are ULXs with nine sources spanning $L_{\rm X} \approx (2\text{--}10) \times 10^{39}$ erg s^{-1} for NGC 3310 (Smith et al. 2012) and roughly a dozen sources with $L_{\rm X} \approx (2\text{--}60) \times 10^{39}$ erg s^{-1} in NGC 3256 (Lira et al. 2002). These ULXs dominate the galaxy-wide emission from $\approx 2\text{--}8$ keV and are expected to provide majority contributions to the non-AGN emission in the $\approx 8\text{--}30$ keV bandpass. We therefore chose to model the broadband 0.3–30 keV spectra of the galaxies using the sum of thermal and power-law components to account for the hot gas and ULXs, respectively.

For each galaxy, we tested for the presence of 2–3 thermal components, in which the absorption of each component increases with increasing temperature. Such a trend has been seen in spatially resolved starburst galaxies like M82, NGC 253, and past studies of NGC 3256, in which the hottest, most obscured components are located in the nuclear regions and the cooler, unobscured plasmas extend to larger galaxy-wide scales (e.g., Strickland et al. 2000; Pietsch et al. 2001; Lira et al. 2002; Strickland & Heckman 2007, 2009; Ranalli et al. 2008). We made use of the spatial resolving power of *Chandra* to better inform our estimates of the diffuse emission component. To this end, we extracted *Chandra* "diffuse component" spectra from the galaxies after removing the bright point-source populations. In this exercise, we excluded events from regions that were within 1.5× the radius of the 90% encircled-energy fraction PSFs of all bright *Chandra* detected point sources (see Section 4.2 below for details on the *Chandra* detected point-source population) and extracted events from within the same apertures used for the galaxy-wide spectra discussed above. The resulting diffuse component spectra are expected to be dominated by hot gas and unresolved, low luminosity X-ray point-sources. We note that the bright X-ray point-source densities are highest in the central regions of the galaxies where star formation is highest. It is in these same regions where we expect to have the hottest X-ray-emitting gas associated with the starbursts. For NGC 3256 and NGC 3310, the removal of these regions will therefore likely result in the removal of a significant fraction of the emission from the hottest gas component.

As a first step, we fit the diffuse, point-source-subtracted *Chandra* spectra using two thermal components (`apec` in `XSPEC`; Smith et al. 2001) plus a single power-law (accounting for unresolved point sources), to determine the temperatures of the galaxy-wide hot gas.[15] In the top portion of Table 1, we list the best-fit temperatures that result from this process. Similar to the results presented by Jenkins et al. (2004), we find best-fitting temperatures of $kT \approx 0.3$ and 0.9 keV for NGC 3256; however, we find that much cooler temperatures of $kT \approx 0.2$ and 0.3 keV were required for NGC 3310, with the latter component being more absorbed and intrinsically powerful than the former component.

Next, for each galaxy, we modeled the full galaxy-wide *Chandra* plus *NuSTAR* spectrum using the two thermal components (with temperatures fixed at the previous best-fit values) plus a third, hotter ($kT \gtrsim 1$ keV) and more obscured thermal component and a non-thermal component to model emission from the point source population. For the point source spectral component, we tested both a single and broken power-law model to see if breaks (e.g., at $E \approx 3\text{--}8$ keV) were preferred, as is most often the case for individual ULX spectra (e.g., Gladstone et al. 2009; Bachetti et al. 2013; Lehmer et al. 2013; Rana et al. 2014; Wik et al. 2014a). Since the point-source spectra of our galaxies contain the conglomerated summed emission from primarily ULXs, we do not report fits using more complex models that contain detailed physical treatment of individual accretion disks and coronae (e.g., `diskbb`, `diskpbb`, `diskpn`, `comptt`, `eqpair`, and `dkbbfth`). In Table 1, we provide the best-fitting parameters for fits to the *Chandra* plus *NuSTAR* spectra that include the two temperature plasma (with fixed temperatures) component, plus an absorbed hotter component (in the case of NGC 3256 only), plus an absorbed single or broken power-law component. In the bottom panels of Figure 4 we display the residuals to these fits.

For NGC 3256, we find that the sum of the diffuse component plus a single absorbed ($N_{\rm H} \approx 3 \times 10^{22}$ cm^{-2}) power-law ($\Gamma \approx 2.6$) and an absorbed hot (≈ 1 keV) plasma component were sufficient to obtain a good fit to the 0.3–30 keV spectrum. The absorbed hot plasma component was implemented to fit a notable Fe-line feature in the *NuSTAR* spectrum at $\approx 6.4\text{--}6.8$ keV. Such a feature is also notable in the *Chandra* spectrum of the full galaxy but not the diffuse region with point sources removed (see above). Further analysis indicates that the Fe emission photons are concentrated in a region within ≈ 20 arcsec of the nucleus, where most of the X-ray detected point sources are located. This component was not in our diffuse, point-source-subtracted *Chandra* spectrum because of the spatial coincidence with point sources. We note that X-ray binaries and obscured AGNs may also provide some contribution to such a feature. However, given the steepness of the galaxy-wide spectral slope above $\gtrsim 8$ keV, it is unlikely that the Fe-line is powered by an obscured AGN, which would have a harder spectral slope ($\Gamma \approx 1.5\text{--}2.0$; see Section 4.3). Replacing the single power-law with a broken power-law does

---

[15] We modeled the point-source-subtracted *Chandra* spectra using `XSPEC` model `tbabs*(apec + tbabs*apec + tbabs*powerlaw)` and fixed the initial absorption to Galactic and the power-law spectral slope to $\Gamma = 1.8$, a value consistent with that of bright X-ray binaries (e.g., Mineo et al. 2012a). The `apec` component abundances were fixed to solar.

Table 1
Best-fit Parameters for Full-galaxy Spectra of NGC 3256 and NGC 3310

PARAMETER	UNIT	NGC 3256	NGC 3310
		Chandra Only Fit: Point-source Subtracted Diffuse Emission[a]	
$N_{H,Gal}$	10^{22} cm^{-2}	0.096	0.011
kT_1	keV	$0.33^{+0.06}_{-0.04}$	0.2 ± 0.1
$N_{H,2}$	10^{22} cm^{-2}	$0.74^{+0.09}_{-0.04}$	$0.6^{+0.2}_{-0.1}$
kT_2	keV	$0.90^{+0.06}_{-0.08}$	$0.28^{+0.08}_{-0.08}$
		Chandra + *NuSTAR* Galaxy-wide Fit: Diffuse Emission Plus Non-thermal Point Sources[b]	
$N_{H,3}$	10^{22} cm^{-2}	115^{+178}_{-93}	…
kT_3	keV	$1.0^{+2.4}_{-0.4}$	…
$N_{H,PL}$	10^{22} cm^{-2}	$3.0^{+1.9}_{-1.2}$	$0.89^{+0.30}_{-0.56}$
Γ_1	…	…	$2.07^{+0.23}_{-0.59}$
E_{break}	keV	…	$4.70^{+0.72}_{-1.21}$
Γ_2	…	2.64 ± 0.20	$2.65^{+0.10}_{-0.14}$
A_{kT_1}	…	$(1.77 \pm 0.20) \times 10^{-4}$	$(1.15 \pm 0.32) \times 10^{-4}$
A_{kT_2}	…	$(1.29^{+0.08}_{-0.10}) \times 10^{-3}$	$2.85^{+0.28}_{-0.55} \times 10^{-4}$
A_{kT_3}	…	$4.0^{+1046}_{-4.0} \times 10^{-2}$	…
A_{PL}	Photons keV^{-1} cm^{-2} s^{-1} at 1 keV	$4.6^{+1.8}_{-2.5} \times 10^{-4}$	$7.4^{+2.9}_{-3.8} \times 10^{-4}$
χ^2_{red}	…	1.09	0.98
ν	(Degrees of freedom)	159	192
f_X (10–30 keV)	10^{-13} erg cm^{-2} s^{-1}	1.33 ± 0.03	5.9 ± 0.4
L_X (10–30 keV)	10^{40} erg s^{-1}	1.99 ± 0.05	2.8 ± 0.2

Note. All quoted errors are at the 90% confidence level.

[a] Fits to the point-source subtracted diffuse *Chandra* spectra were performed using XSPEC model tbabs$_{Gal}$*(apec$_1$+tbabs $^*_2$apec$_2$+tbabs $_{PL}$*pow) to obtain values of T_1, T_2, and $N_{H,2}$. In this process the power-law had a fixed photon index of $\Gamma = 1.8$ and all thermal models assumed solar abundances. Values of T_1, T_2, and $N_{H,2}$ were subsequently fixed when fitting the *Chandra* + *NuSTAR* galaxy-wide spectra, where their normalizations were free to vary.

[b] The galaxy-wide *Chandra* + *NuSTAR* spectra were fit using XSPEC models tbabs$_{Gal}$*(apec$_1$+tbabs $^*_2$apec$_2$+tbabs $^*_3$apec$_3$+tbabs $_{PL}$*bknpo) and tbabs$_{Gal}$*(apec$_1$+tbabs $^*_2$apec$_2$+tbabs $_{PL}$*pow) for NGC 3256 and NGC 3310, respectively.

not improve the quality or change the character of the fit (see lower panels of Figure 4 left). Since the thermal components in the galaxy dominates the ≈0.3–2.5 keV emission in NGC 3256, a true break in the power-law component could be masked if it resides at $E \lesssim 3$ keV.

For NGC 3310, we find that the diffuse component plus a broken power-law model provides the best fit to the data; no additional absorbed hotter component was required to fit the spectrum, as we do not see clear evidence for an Fe-line. The best-fitting slopes ($\Gamma_1 \approx 2.1$ and $\Gamma_2 \approx 2.7$) and energy break ($E_{break} \approx 4.7$ keV) are within the range of values found for ULXs (e.g., Gladstone et al. 2009). In contrast to NGC 3256, which had strong emission features related to hot gas out to $E \approx 3$ keV, we find that the overall spectrum of NGC 3310 above ≈1 keV is dominated by the point-source population. As we will discuss in more detail below, the SFR-normalized point-source emission in NGC 3310 is a factor of ≈3–10 times higher compared to other starburst galaxies studied in our program (i.e., NGC 253, NGC 3256, and M83). The relatively strong emission from the point-source population may therefore be masking lower-intensity line features that would betray the presence of a hot X-ray plasma or an obscured AGN (e.g., Fe emission-lines). If NGC 3310 harbors an obscured AGN, it is almost certainly of low luminosity and is likely to provide only a minor perturbation on the non-AGN emission in the *NuSTAR* band. We return to the discussion of the potential for AGNs in both NGC 3256 and NGC 3310 in Section 4.3 below when we discuss the *Chandra* properties of the nuclear sources in detail.

4.2. Chandra Point-source Analyses

Our joint *NuSTAR* and *Chandra* spectral analyses indicate that the galaxy-wide 0.3–30 keV emission from NGC 3256 and NGC 3310 are dominated by the combination of hot gas and ULX populations, with no obvious signatures of luminous AGN. In this section, we gain further insight into the X-ray emitting populations in these galaxies by performing basic *Chandra* spectral analyses of the detected point-sources and diffuse emission.

For each galaxy, we identified point sources that had >20 0.5–7 keV counts that were also detected in the 2–7 keV band images using wavdetect at a false-positive probability threshold of 10^{-5}; these sources were candidates for performing basic spectral fits. For NGC 3256 and NGC 3310, we found 7 and 9 sources, respectively, that satisfied these criteria; the locations of these sources are annotated in Figure 3. Taken together, these sources respectively provide ≈42% and ≈79% of the 2–7 keV *Chandra* net counts within the total galaxy apertures defined in Section 4.1. For these sources, we extracted the *Chandra* spectra and fit them using both an absorbed power-law model (powerlaw) and an absorbed multicolor accretion disk (diskbb; Shakura & Sunyaev 1973; Mitsuda et al. 1984). In this procedure, point-sources were extracted from circular regions that encompassed 90% of the encircled energy of the PSF (≈2 arcsec in radius for all sources). We utilized the same background regions used in Section 4.1 to estimate background spectra for the sources. As such, some source regions will contain background related to diffuse emission. Since the exposures are relatively shallow and

diffuse emission gradients are high, we chose not to attempt to model the local background component. When relevant, we have qualified interpretations of the *Chandra* source spectra with this limitation. Given the small number of counts per source (33–329 0.5–7 keV counts), all spectral fits were performed by minimizing the Cash statistic (cstat; Cash 1979) using spectra binned to a minimum of one count per channel.

In Table 2, we present the best-fit parameters for the point-source spectral fits. We note that the parameters in Table 2 provide only a basic description of the data and are not well constrained, e.g., due to degeneracies between column density and spectral slope or inner disk temperature. In particular, for sources that were located near the nuclei of the galaxies, some contributions from hot gas are expected, which will steepen the inferred spectral slopes. In the majority of cases, a simple power-law provided an acceptable fit to the spectra; we find a slight ($\approx 1\,\sigma$ level) statistical preference for the diskbb model for sources 1 and 9 of NGC 3310. The luminosity range of the point-source populations cover $L_{2-10\,\text{keV}} = (3–20) \times 10^{39}\,\text{erg s}^{-1}$, indicating that if all sources are discrete objects, then they are all in the ULX range of luminosities. The photon indices for the point sources range from $\Gamma = 0.4$–3.6 (median $\langle \Gamma \rangle = 1.8$), with only source 3 in NGC 3310 having $\Gamma < 1.5$ at $>90\%$ confidence. As we will discuss in the next section, source 3 is coincident with the nuclear region in NGC 3310 and is a candidate obscured AGN.

4.3. Contributions from Nuclear Sources and Potential AGNs

Both NGC 3256 and NGC 3310 contain *Chandra* detected point-like sources coincident with their galactic nuclei (NGC 3256 source 4 and NGC 3310 source 3); however, for NGC 3256, we only detect the northern nucleus and not the southern nucleus. In this section, we investigate the nature of the sources coincident with the nuclei using *Chandra* spectral constraints and discuss their potential contributions to the 0.3–30 keV spectra.

For NGC 3256, there is a clear detection of the northern nucleus, which is the brightest point-like source in our *Chandra* catalog (source 4). Using a deeper $\approx 30\,\text{ks}$ *Chandra* exposure (ObsID 835), Lira et al. (2002) found that the nuclear emission is clearly extended, suggesting that the emission must include extended and/or multiple point-sources. From Table 2, we see the *Chandra* spectrum of this source is fit well with a steep power-law ($\Gamma = 2.8 \pm 0.4$) with modest absorption ($N_{\text{H}} \approx 4 \times 10^{21}\,\text{cm}^{-2}$). Such a steep photon index is uncharacteristc of AGNs, which typically span $\Gamma \approx 1$–2.2. We refit the spectrum using only the 3–7 keV range, to mitigate any biases in the spectral fit due to soft emission from the hot gas, which will inevitably be coincident with our spectral extraction of this region. The resulting best-fit photon index remained unchanged, indicating that there is no evidence for an emerging hard X-ray AGN in this region. This result is consistent with previous studies that have concluded that the northern nucleus in NGC 3256 is powered almost exclusively by star formation activity (e.g., Lira et al. 2002; Jenkins et al. 2004; Sakamoto et al. 2014). In Figure 4, we show the contribution from the northern nucleus extrapolated through to the *NuSTAR* band. Based on this extrapolation and the global fit presented in Section 4.1, we estimate that this source will contribute $\approx 4\%$–10% of the galaxy-wide emission across the full 0.3–30 keV band.

Our 16 ks *Chandra* observation of NGC 3256 did not yield a clear detection of the southern nucleus (location indicated in the left panel of Figure 3), which has previously been shown to have submm and near-infrared evidence for a collimated outflow, potentially due to an AGN that is currently inactive (e.g., Emonts et al. 2014; Sakamoto et al. 2014). Two previous deeper $\approx 25\,\text{ks}$ archival *Chandra* exposures (ObsIDs 835 and 3569) reveal clear detections of a source coincident with the southern nucleus, suggesting that the source does produce powerful, albeit heavily obscured, X-ray emission at the $\approx 10^{40}\,\text{erg s}^{-1}$ level (in the 0.3–10 keV band). Using the *Chandra* exposure from ObsID 835, as well as radio, near-IR, and optical data, Lira et al. (2002) showed that this source is likely to be a low luminosity AGN that does not provide a significant contribution to the total X-ray emission of the galaxy. No evidence was found implicating a luminous, heavily obscured AGN (e.g., Fe-line emission). The non-detection of the southern nucleus in our 16 ks *Chandra* exposure indicates a change in the southern source with respect to the previous two observations. In 2000 January 5 and 2003 May 23, the southern source was detected with similar 2–7 keV *Chandra* count-rates of $(2.7 \pm 0.3) \times 10^{-3}$ and $(2.9 \pm 0.3) \times 10^{-3}\,\text{cnts s}^{-1}$, respectively. Whereas the 3σ upper limit on the 2–7 keV *Chandra* count-rate in our 2014 August 28 observation is $<1.2 \times 10^{-3}\,\text{cnts s}^{-1}$, indicating a factor of $\gtrsim 2.0$–2.5 times decline in the southern source hard-band intensity. As shown by our *NuSTAR* spectrum, the steep spectral slope of the full galaxy persists out to at least $\approx 30\,\text{keV}$, limiting the possible contributions from a hard southern nuclear AGN. This implies that if there is an AGN associated with the southern nucleus, it is likely to be of low luminosity.

To place more stringent constraints on the spectral properties of the southern nucleus, we combined the previous two *Chandra* observations of NGC 3256 to create a merged $\approx 50\,\text{ks}$ data set. We extracted the merged spectrum of the southern nuclear source and performed spectral fitting in XSPEC. The spectrum can be fit well by a simple power-law model with an inverted photon index of $\Gamma \approx -0.1$; the best-fit model implies a 2–10 keV luminosity of $L_{2-10\,\text{keV}} \approx 10^{40}\,\text{erg s}^{-1}$. It is likely that the spectrum contains both contributions from hot gas and a heavily obscured power-law source coincident with the nuclear region. The black hole mass for the southern nucleus is on the order of $\sim 10^{7}\,M_{\odot}$ (e.g., Alonso-Herrero et al. 2013), implying an Eddington luminosity of $\sim 10^{45}\,\text{erg s}^{-1}$. If the southern nucleus is indeed an AGN it would therefore have $L_{2-10\,\text{keV}}/L_{\text{Edd}} \sim 10^{-5}$, and the expected intrinsic spectral slope of this source would be between $\Gamma = 1.5$–2.0 (Younes et al. 2011). Using these constraints, we fit the spectrum of the southern nucleus using an absorbed plasma plus an absorbed power-law model (tbabs* apec+ tbabs*powerlaw in XSPEC). We held the plasma temperature fixed at 0.6 keV (see Lira et al. 2002 for motivation) and the power-law slope fixed at $\Gamma = 1.8$ and fit for the component normalizations and obscuring columns. This model yielded a good fit to the data for column densities $N_{\text{H,gas}} \approx 10^{22}\,\text{cm}^{-2}$ and $N_{\text{H,PL}} \approx 5 \times 10^{22}\,\text{cm}^{-2}$.

In the left panel of Figure 4, we show the *Chandra* spectrum and best-fitting model of the southern nucleus of NGC 3256 from the previous two observations when the source was detectable (*orange data and curve*). The data and model have been scaled down by a factor of 2.5 to show the upper limit to our 2014 observation (see above). Based on an extrapolation of

Table 2
Chandra Point-source Properties

Source ID (1)	α_{J2000} (hr) (2)	δ_{J2000} (degree) (3)	powerlaw $N_{H,int}$ (10^{22} cm^{-2}) (4)	Γ (5)	C (6)	diskbb $N_{H,int}$ (10^{22} cm^{-2}) (7)	kT_{in} (keV) (8)	C (9)	ν (10)	$\log f_{2-10\,keV}$ (log erg cm^{-2} s^{-1}) (11)	$\log L_{2-10\,keV}$ (log erg s^{-1}) (12)	Net Counts (0.5–7 keV) (13)	Note (14)
						NGC 3256							
1	10 27 50.0	−43 54 19.8	$0.02^{+0.38}_{-0.02}$	$1.4^{+0.9}_{-0.5}$	43	< 0.16	$1.9^{+4.7}_{-0.7}$	45	32	−13.5	39.6	43 ± 7	⋯
2	10 27 50.6	−43 54 19.8	< 0.38	$1.2^{+0.7}_{-0.3}$	60	< 0.20	$2.0^{+2.1}_{-0.7}$	60	55	−13.2	39.9	67 ± 8	⋯
3	10 27 50.8	−43 54 15.2	$0.37^{+0.37}_{-0.32}$	$2.2^{+0.4}_{-0.3}$	44	$0.08^{+0.24}_{-0.08}$	$1.2^{+0.7}_{-0.3}$	46	52	−13.5	39.7	71 ± 8	⋯
4	10 27 51.2	−43 54 13.9	$0.36^{+0.14}_{-0.12}$	$2.8^{+0.4}_{-0.4}$	123	$0.04^{+0.09}_{-0.04}$	$0.8^{+0.1}_{-0.1}$	126	140	−13.1	40.1	329 ± 18	Nucleus (N)
5	10 27 51.6	−43 54 09.3	$0.32^{+0.18}_{-0.16}$	$2.9^{+0.6}_{-0.6}$	65	$0.02^{+0.11}_{-0.02}$	$0.8^{+0.2}_{-0.2}$	69	88	−13.5	39.6	139 ± 12	⋯
6	10 27 51.8	−43 54 13.3	$0.55^{+0.25}_{-0.21}$	$3.6^{+0.8}_{-0.8}$	60	$0.18^{+0.15}_{-0.13}$	$0.6^{+0.2}_{-0.1}$	63	68	−13.7	39.4	118 ± 11	⋯
7	10 27 55.1	−43 54 46.6	< 0.71	$0.5^{+1.4}_{-0.8}$	33	< 0.43	>1.35	33	25	−13.1	40.0	33 ± 6	⋯
						NGC 3310							
1	10 38 43.3	+53 31 02.0	$0.22^{+0.15}_{-0.14}$	$2.3^{+0.4}_{-0.4}$	31	$0.01^{+0.10}_{-0.01}$	$0.9^{+0.2}_{-0.2}$	27	23	−12.8	39.8	168 ± 13	⋯
2	10 38 44.8	+53 30 04.3	$0.55^{+0.54}_{-0.49}$	$1.6^{+0.7}_{-0.7}$	12	$0.34^{+0.37}_{-0.16}$	$1.7^{+2.0}_{-0.6}$	11	10	−12.7	40.0	152 ± 12	⋯
3	10 38 45.8	+53 30 12.2	$0.30^{+0.71}_{-0.30}$	$0.4^{+0.7}_{-0.6}$	9	$0.58^{+0.35}_{-0.30}$	>10	10	8	−12.4	40.3	174 ± 13	Nucleus
4	10 38 46.0	+53 30 04.8	$0.71^{+0.42}_{-0.38}$	$1.8^{+0.6}_{-0.6}$	9	$0.40^{+0.28}_{-0.25}$	$1.5^{+0.9}_{-0.4}$	10	16	−12.6	40.1	131 ± 11	⋯
5	10 38 46.5	+53 30 38.3	$0.84^{+0.51}_{-0.46}$	$2.0^{+0.7}_{-0.6}$	14	$0.51^{+0.35}_{-0.31}$	$1.3^{+0.7}_{-0.3}$	12	12	−12.7	40.0	142 ± 12	⋯
6	10 38 46.6	+53 30 13.7	$0.59^{+0.67}_{-0.59}$	$1.7^{+0.8}_{-0.8}$	2	$0.24^{+0.44}_{-0.24}$	$1.9^{+2.4}_{-0.7}$	3	8	−12.8	39.9	130 ± 11	⋯
7	10 38 46.7	+53 30 07.8	< 0.22	$1.9^{+0.7}_{-0.4}$	5	< 0.08	$0.8^{+0.3}_{-0.2}$	8	7	−13.1	39.5	213 ± 15	⋯
8	10 38 47.2	+53 30 27.9	$0.28^{+0.33}_{-0.28}$	$1.8^{+0.6}_{-0.6}$	13	$0.04^{+0.22}_{-0.04}$	$1.5^{+0.7}_{-0.4}$	13	10	−12.9	39.8	121 ± 11	⋯
9	10 38 50.2	+53 29 26.0	$0.46^{+0.34}_{-0.32}$	$2.0^{+0.7}_{-0.7}$	22	$0.25^{+0.24}_{-0.22}$	$1.0^{+0.5}_{-0.3}$	19	12	−12.9	39.8	294 ± 17	⋯

Note. All quoted errors on fit parameters indicate 90% confidence intervals, while quoted errors associated with net counts are 1σ. Column (1): Source ID. Column (2) and (3): R.A. and decl., respectively, based on *Chandra* source location. Column (4)–(6) provide parameters to spectral fits for a power-law with intrinsic absorption model. Column (4): intrinsic absorption column density in units of 10^{22} cm^{-2}. Column (5): power-law photon index. Column (6): minimum `cstatistic` C. Column (7)–(9) provide parameters to spectral fits for a multicolor accretion disk (`diskbb`) with intrinsic absorption model. Column (7): intrinsic absorption column density in units of 10^{22} cm^{-2}. Column (8): Best-fitting inner accretion disk temperature (kT_{in}) in units of keV. Column (9): minimum `cstatistic` C. Column (10) Number of degrees of freedom for both power-law and multicolor accretion disk fits. Column (11) and (12): observed 2–10 keV flux and luminosity based on the best-fitting model. Column (13) Net counts in the 0.5–7 keV *Chandra* band. Column (14): Notes on the individual sources.

this model to the *NuSTAR* band, the southern nucleus is expected to contribute $\lesssim 10\%$–30% of the *NuSTAR* emission at 10–30 keV. Such a low level of AGN activity is insufficient to have any material effect on the overall shape of the galaxy spectrum nor on the constraints presented in Section 4.1 and Table 1. We therefore expect that the 0.3–30 keV spectrum of NGC 3256 is dominated by non-AGN emitting sources (i.e., hot gas and X-ray binaries).

For NGC 3310, a previous ≈ 50 ks *Chandra* observation from 2003 (ObsID 2939) was used by Tzanavaris & Georgantopoulos (2007) to show that there is evidence for an Fe-Kα emission line in the nuclear source (source 3), implying the presence of a hidden AGN. Our ≈ 10 ks *Chandra* observation was too shallow to verify the claimed Fe-Kα feature, which was of low significance ($\approx 2\ \sigma$) in the much deeper 2003 observation. However, we do find that the best-fitting power-law spectral slope of the nuclear point-source $\Gamma \approx 0.4$ is much shallower than the other sources in the galaxy ($\Gamma \approx 1.6$–2.3), and the luminosity of the source ($L_{2–10\,\mathrm{keV}} \approx 10^{40}\ \mathrm{erg\ s^{-1}}$) is the highest of all the point-sources. These facts are consistent with an obscured or low luminosity AGN hypothesis. We note that if we invoke a more complex model appropriate for AGNs that includes both direct and scattered components (e.g., `pexrav` or `MyTorus`; Magdziarz & Zdziarski 1995; Murphy & Yaqoob 2009), the expected contribution to the galaxy-wide emission above 10 keV can quickly approach 100%, and the intrinsic emission could be much higher than the observed luminosity inferred by *Chandra*.

Following a similar approach to that taken for the southern nucleus in NGC 3256, we tested the influence that the nuclear source in NGC 3310 would have on the ≈ 7–30 keV emission, if it were truly an AGN, by extrapolating the *Chandra* spectrum through to the *NuSTAR* band. The black hole mass of NGC 3310 is currently poorly constrained, but has been estimated via gas kinematics to be $\sim (5$–$40) \times 10^6\ M_\odot$, which implies an Eddington luminosity of $\sim (6$–$50) \times 10^{45}\ \mathrm{erg\ s^{-1}}$ (Pastorini et al. 2007). The 2–10 keV luminosity of the source, as measured by *Chandra*, is $L_{2–10\,\mathrm{keV}} \sim 10^{40}\ \mathrm{erg\ s^{-1}}$, implying $L_{2–10\,\mathrm{keV}}/L_{\mathrm{Edd}} \sim 10^{-6}$–$10^{-5}$. From Younes et al. (2011), this implies an intrinsic photon index of $\Gamma = 1.5$–2.2. Following the approach used for the southern nucleus of NGC 3256, we fit the *Chandra* spectrum of the NGC 3310 nuclear source using an absorbed plasma plus an absorbed power-law model (`tbabs*apec+ tbabs*po-werlaw` in XSPEC) with the plasma temperature fixed at 0.3 keV and the power-law slope fixed at $\Gamma = 1.8$. These parameters yielded a good fit to the data for column densities $N_{\mathrm{H,gas}} \approx 5 \times 10^{21}\ \mathrm{cm^{-2}}$ and $N_{\mathrm{H,PL}} \approx 3 \times 10^{22}\ \mathrm{cm^{-2}}$.

In the right panel of Figure 4, we show the *Chandra* spectrum for the nuclear source of NGC 3310 and the best-fit model extrapolated across the full 0.3–30 keV band. It is clear that the nuclear source is expected to provide a non-negligible contribution to the X-ray emission above 4–5 keV. Based on our extrapolated model, the point-source makes a fractional contribution of $\lesssim 3\%$ of the galaxy-wide emission at $E < 2$ keV and reaches a maximum contribution of ≈ 30–100% in the 20–30 keV band. If we revist our fits to the galaxy-wide spectrum performed in section 4.1 and now fix the diffuse component and best-ftting model for the nuclear source, we find that the remaining spectrum associated with the bright point sources can be well characterized by a broken power-law with parameters consistent with those presented in Table 1.

4.4. Spatially Extended NuSTAR Emission for NGC 3310

Although the *NuSTAR* PSF is too large to identify individual X-ray point sources in the galaxies studied here, it is sufficient for identifying extended features due to the ≈ 50 arcsec wide distribution of point sources throughout NGC 3310. To test for extended *NuSTAR* emission, we first constructed a spatial model of the expected *NuSTAR* emission profile within a bandpass that overlapped with *Chandra* (i.e., 4–8 keV), and then tested to see how the *NuSTAR* emission profile changed in a bandpass above the *Chandra* response (i.e., 8–25 keV). If the X-ray SEDs of the underlying point sources were all similar, we would expect the profile to remain the same for the soft and hard bands. Using the positions and relative 4–8 keV *Chandra* count-rates for the point sources, we constructed a model distribution map of *NuSTAR* counts. This map was constructed by co-adding *NuSTAR* PSF images centered at the locations of the *Chandra* point sources, with normalizations scaled by the 4–8 keV *Chandra* count-rates. Throughout this process, our *NuSTAR* PSFs were constructed by accounting for the off-axis angles of the sources and include errors associated with variations in off-axis angle due to the motions of the mast. We note that some relative astrometric offset is expected to be present between the *NuSTAR* and *Chandra* data. In order to estimate this error, we fit Gaussian profiles to both the *NuSTAR* 4–8 keV image emission and the *Chandra*-based model distribution map to identify the location of the peak emission. We then extracted the emission profiles for the images and models and compared them.

In Figure 5, we show the spatial distribution of *NuSTAR* counts for the 4–8 keV and 8–25 keV bands. The expected distributions for the *Chandra*-based model (described above) and an individual point-source PSF model have been overplotted for comparison. By construction, the 4–8 keV *NuSTAR* emission profile follows the *Chandra*-based model well and is statistically inconsistent with a single point source. However, at 8–25 keV, the *NuSTAR* emission profile is more consistent with a single point-source (i.e., the *NuSTAR* PSF) than with the *Chandra*-based model, implying that the central region of NGC 3310 contains a harder X-ray spectrum (across 8–25 keV) compared to point-sources in the outskirts of the galaxy. Our spectral extrapolation of the nuclear source presented in Section 4.3 and Figure 4 (*right*) shows that the fractional contribution that the source makes to the galaxy-wide emission increases with energy. It is also the case that the two sources in the outskirts of the galaxy (sources 1 and 9; see Figure 3 and Table 2) have the steepest spectral slopes out of all nine point sources. Therefore, the hard spectra of the nuclear source and the five relatively hard non-nuclear sources that are within ≈ 20 arcsec of the galactic center are likely to be responsible for the transition to a more point-like emission profile with increasing energy. As we discussed above, we find a steep $\Gamma \approx 2.7$ power-law slope at $E \gtrsim 4$ keV for the galaxy-wide spectrum of NGC 3310, which is steeper than the best-fit single power-law slopes ($\Gamma \approx 0.3$–2.0) derived for all five sources. This implies that, although the spectra of these sources may be intrinsically hard in the *Chandra* band, spectral turnovers at $E \gtrsim 3$–10 keV must be typical of these sources, making it difficult to quantify the relative influences these sources have on the emission measured in the *NuSTAR* band.
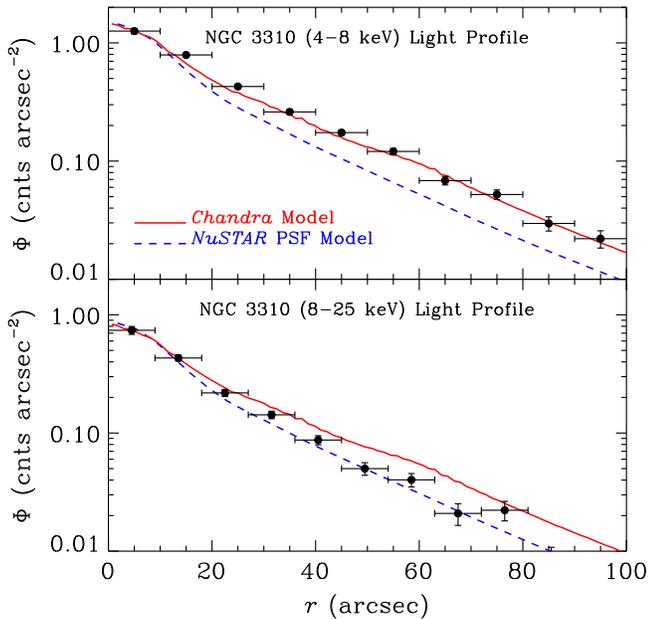
Figure 5. *NuSTAR* light profiles for NGC 3310 in the 4–8 keV (top) and 8–25 keV (bottom) bands. A blurred PSF model (blue dashed curves) and a model based on the relative 4–8 keV *Chandra* point-source brightnesses ("*Chandra* Model"; red solid curves) have been compared with the *NuSTAR* light profiles (black points). We find that the "*Chandra* Model" characterizes well the *NuSTAR* galaxy light profile in the *Chandra* and *NuSTAR* overlapping 4–8 keV bandpass. However, due to the presence of harder sources in the central region of the galaxy, as compared with sources in the outskirts, the 8–25 keV light profile becomes more point-like. Such a result could be explained by the presence of an obscured AGN and/or harder ULXs in the central region of the galaxy.

5. DISCUSSION

We have utilized nearly simultaneous *Chandra* and *NuSTAR* observations of the powerful local starburst galaxies NGC 3256 and NGC 3310 to investigate the nature of the X-ray-emitting components across the broad 0.3–30 keV bandpass. Similar to previous *XMM-Newton* and *Chandra* studies, we find significant $kT \approx 0.2$–1 keV plasma emission that dominates the spectra of these galaxies out to ≈ 3 and ≈ 1 keV for NGC 3256 and NGC 3310, respectively. At the higher energies probed by *NuSTAR* ($E \gtrsim 3$ keV), we find the majority of the emission is produced by populations of the brightest 5–10 ULXs. The cumulative spectra of both galaxies exhibit steep power-law slopes ($\Gamma \approx 2.6$–2.7) above ≈ 3–6 keV that are similar to those found in *NuSTAR* studies of individual ULXs, implying that no strong hard component exists for either galaxy. This places stringent limits on the influence of possible AGN candidates in both galaxies, which are expected to have much flatter spectral slopes in this band. Sensible extrapolations of the *Chandra* spectra of AGN candidates in these galaxies, the southern nucleus of NGC 3256 and the nucleus of NGC 3310, indicate that these candidates provide only minority contributions to the galaxy-wide *NuSTAR* emission out to 30 keV. Regardless of extrapolation assumptions, our constraints indicate that the supermassive black holes in these galaxies are of low intrinsic luminosity and are accreting at the $\lesssim 10^{-6}$–10^{-5} Eddington levels. Our spectral constraints on NGC 3256 and NGC 3310 therefore provide first measurements of the 0.3–30 keV spectra of the non-AGN X-ray emitting populations within powerful starburst galaxies with high-sSFRs.

In Figure 6, we show the SFR-normalized best-fitting 0.3–30 keV SEDs (i.e., νL_{ν}/SFR) of NGC 3256 and NGC 3310. For comparison, we also provide best-fit models for M83 (Yukita et al. 2015, in preparation) and NGC 253 (Wik et al. 2014a), which were also constrained using nearly simultaneous observations with *Chandra/XMM-Newton* and *NuSTAR*. The displayed SEDs have not been corrected for intrinsic absorption and are therefore representative of the *observed* X-ray spectra. In the low-energy regime ($E \lesssim 2$–3 keV), all four galaxies have significant contributions from line-emitting hot plasmas. With the exception of NGC 253 (*orange curve*) the SFR-normalized gas components have similar normalizations around ≈ 1 keV, consistent with previous studies that have found a direct scaling of the hot gas emission with SFR (see, e.g., Mineo et al. 2012b). Compared with the other three galaxies, NGC 253 is relatively edge-on ($i \approx 80°$), and therefore absorption is likely playing a role in the apparent deficit of hot gas emission in the galaxy.

At higher energies, $E \approx 3$–30 keV, we find that all galaxies, except for NGC 3310 (see discussion below), have SFR-normalized SEDs that are in good agreement with each other. For all four galaxies, the steepening of the spectral slope in the ≈ 6–30 keV range is clearly apparent. For M83, it appears that the spectral slope in this regime is somewhat steeper than it is for the other three galaxies. As discussed by Yukita et al. (2015, in preparation), the spectral shape of M83 is strongly influenced by a single variable ULX (see also Soria et al. 2012 for details on this source). For comparison, we have overlaid in Figure 6 the *NuSTAR*-constrained SEDs (scaled to the mean starburst galaxy emission at 5 keV) of the ULX NGC 1313 X-1 (Bachetti et al. 2013), the luminous black hole X-ray binary GRS 1915+105 in the low/hard state (Miller et al. 2013), and the Compton-thick AGN in Arp 299 (Ptak et al. 2014). From this illustration, it is clear that the >10 keV starburst galaxy SEDs, including the turnover in spectral slope, are very similar to the SED of NGC 1313 X-1, a likely super-Eddington accreting ULX. Given the fact that ULXs clearly dominate the point source emission from this galaxy population, our observations constrain the average spectral shape for the ULX population, in general.

Interestingly, for NGC 3310, we observe a clear factor of ≈ 3–10 times excess X-ray emission per unit SFR over the ≈ 6–30 keV range. The excess is the result of an overabundance of ULXs in the galaxy compared to typical galaxies. From Mineo et al. (2012a), we expect that there would be ≈ 1–4 ULXs given the SFR of NGC 3310 (SFR ≈ 6 $M_{\odot}$ yr^{-1}); however, 9 ULXs are clearly detected, indicated a significant excess in both the X-ray emission and the number of ULXs. In general, an excess of luminous X-ray binaries can be explained by either (1) a star formation history that is heavily weighted toward an epoch when ULXs are expected to be most luminous due to the presence of the most massive donor stars (≈ 5–10 Myr) and/or (2) star formation that is happening in low-metallicity environments, in which an excess population of black holes form (e.g., Linden et al. 2010).

HST-based studies of the young star cluster properties in NGC 3310, using SED fitting of UV-to-near-IR *HST* data, indicate a peak intensity in the recent star formation history around ≈ 30 Myr ago (de Grijs et al. 2003a, 2003b), well past the peak of ULX activity. Furthermore, similar star-cluster ages are also seen in NGC 3256 (e.g., Trancho et al. 2007), which suggests that the excess of luminous X-ray binaries in NGC
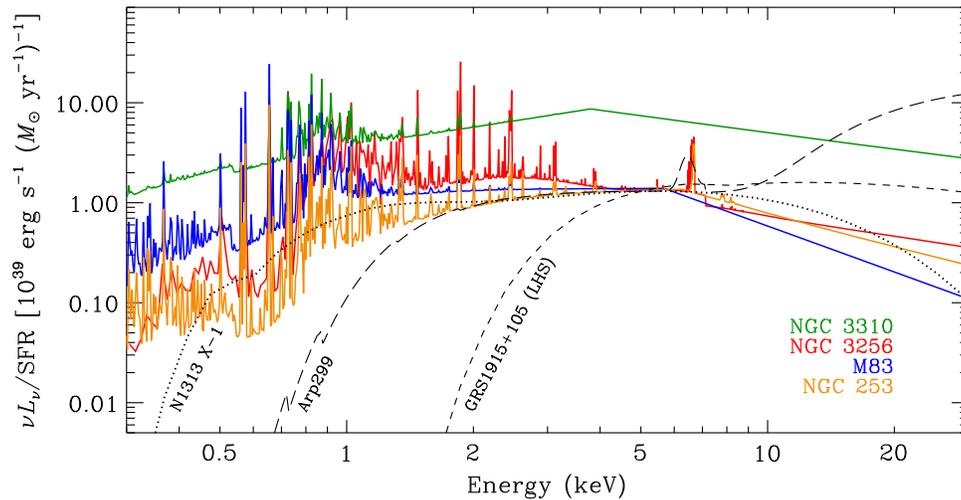
Figure 6. SFR-normalized 0.3–30 keV SEDs for NGC 3256 (red), NGC 3310 (green), NGC 253 (orange), and M83 (blue). For illustrative purposes, we have displayed only the best-fit SEDs to the nearly simultaneous *Chandra*/*XMM-Newton* plus *NuSTAR* data. NGC 253 and M83 fits are taken from the best-fit models presented in Wik et al. (2014a) and Yukita et al. (2015, in preparation). For comparison, we have shown *NuSTAR* constrained SEDs for the ULX NGC 1313 X-1 (dotted curve; Bachetti et al. 2013), the luminous black hole X-ray binary GRS 1915+105 in the low/hard state (short-dashed curve; Miller et al. 2013), and the Compton-thick AGN in Arp 299 (long-dashed curve; Ptak et al. 2014); these SEDs have been normalized to νL_ν/SFR $= 1.3 \times 10^{39}$ erg s^{-1} $(M_\odot$ yr$^{-1})^{-1}$ at 5 keV for ease of comparison. In this representation, a power-law SED with photon-index $\Gamma = 2$ is a flat line. It is clear that all four galaxies here show steepening in their SEDs above $\approx$3–6 keV, where their spectral slopes reach $\Gamma \approx 2.5$–3.0 due primarily to the ULX population. These constraints indicate that the ULX population on average has a similar spectral shape to that of super-Eddington accreting sources like NGC 1313 X-1.

3310 is unlikely to be caused by differences in recent star formation history alone. By contrast, the metallicity distribution of young star clusters in NGC 3310 has been estimated to peak at $Z \approx 0.4\ Z_\odot$ (de Grijs et al. 2003a, 2003b), compared with $Z \approx 1.5\ Z_\odot$ for M83, NGC 253, and NGC 3256 (e.g., Zaritsky et al. 1994; Boselli et al. 2002; Trancho et al. 2007; Bresolin et al. 2005). The relatively low metallicity in NGC 3310 is the result of the recent cannibalization of a low-metallicity dwarf galaxy that triggered the current star formation event. It is therefore plausible that the lower metallicity of NGC 3310 is the driving mechanism behind the excess of ULXs per unit SFR in this galaxy. Indeed, past studies of both the number of ULXs and galaxy-wide X-ray luminosity per unit SFR have revealed excesses at low metallicities (e.g., Mapelli et al. 2009; Basu-Zych et al. 2013b; Prestwich et al. 2013; Brorby et al. 2014). From the population synthesis models from Fragos et al. (2013b), galaxies with $Z \approx 1.5\ Z_\odot$ and $0.4\ Z_\odot$ are predicted to have SFR-normalized 2–10 keV luminosities of $L_{2-10\ \mathrm{keV}}$/SFR $= (1.1$–$3.4) \times 10^{39}$ and $(3.5$–$11.2) \times 10^{39}$ erg s^{-1}, respectively (e.g., see their Figure 2). We measure corresponding values of $L_{2-10\ \mathrm{keV}}$/SFR $= 2.1 \times 10^{39}$ and 7.3×10^{39} erg s^{-1}, respectively, in very good agreement with the theoretical model predictions. We therefore favor metallicity as being the dominant underlying factor responsible for the observed $\approx$3–10 times excess X-ray emission per unit SFR in NGC 3310; however, future investigations of the properties of the immediate environments (i.e., characteristic stellar ages and metallicities) near the ULXs would help to better discriminate the roles that age and metallicity play in producing the excess ULX population.

REFERENCES

Alonso-Herrero, A., Pereira-Santaella, M., Rieke, G. H., et al. 2013, ApJ, 765, 78
Alonso-Herrero, A., Pereira-Santaella, M., Rieke, G. H., & Rigopoulou, D. 2012, ApJ, 744, 2
Alonso-Herrero, A., Rieke, G. H., Rieke, M. J., & Scoville, N. Z. 2002, AJ, 124, 166
Bachetti, M., Rana, V., Walton, D. J., et al. 2013, ApJ, 778, 163
Balick, B., & Heckman, T. 1981, A&A, 96, 271
Basu-Zych, A. R., Lehmer, B. D., Hornschemeier, A. E., et al. 2013a, ApJ, 762, 45
Basu-Zych, A. R., Lehmer, B. D., Hornschemeier, A. E., et al. 2013b, ApJ, 774, 152
Bell, E. F., McIntosh, D. H., Katz, N., & Weinberg, M. D. 2003, ApJS, 149, 289
Boselli, A., Lequeux, J., & Gavazzi, G. 2002, A&A, 384, 33
Bresolin, F., Schaerer, D., González Delgado, R. M., & Stasińska, G. 2005, A&A, 441, 981
Brorby, M., Kaaret, P., & Prestwich, A. 2014, MNRAS, 441, 2346
Calzetti, D. 2013, Secular Evolution of Galaxies (Cambridge: Cambridge Univ. Press), 419
Cash, W. 1979, ApJ, 228, 939
Chandar, R., Leitherer, C., Tremonti, C. A., et al. 2005, ApJ, 628, 210
Cicone, C., Maiolino, R., Sturm, E., et al. 2014, A&A, 562, A21
Colbert, E. J. M., Heckman, T. M., Ptak, A. F., Strickland, D. K., & Weaver, K. A. 2004, ApJ, 602, 231
de Grijs, R., Anders, P., Bastian, N., et al. 2003b, MNRAS, 343, 1285
de Grijs, R., Fritze-v. Alvensleben, U., Anders, P., et al. 2003a, MNRAS, 342, 259

de Vaucouleurs, G., de Vaucouleurs, A., Corwin, H. G., et al. 1991, Third Reference Catalogue of Bright Galaxies, 1-3, XII (Berlin: Springer), 2069

Díaz, A. I., Álvarez, M. Á, Terlevich, E., et al. 2000, MNRAS, 311, 120

Dickey, J. M., & Lockman, F. J. 1990, ARA&A, 28, 215

Done, C., Gierliński, M., & Kubota, A. 2007, A&ARv, 15, 1

Doyon, R., Joseph, R. D., & Wright, G. S. 1994a, ApJ, 421, 101

Doyon, R., Wright, G. S., & Joseph, R. D. 1994b, ApJ, 421, 115

Elmegreen, D. M., Chromey, F. R., McGrath, E. J., & Ostenson, J. M. 2002, AJ, 123, 1381

Emonts, B., Piqueras-Lopez, J., Colina, L., et al. 2014, arXiv:1409.4468

Fabbiano, G. 2006, ARA&A, 44, 323

English, J., Norris, R. P., Freeman, K. C., & Booth, R. S. 2003, AJ, 125, 1134

Fragos, T., Lehmer, B. D., Naoz, S., Zezas, A., & Basu-Zych, A. 2013b, ApJL, 776, L31

Fragos, T., Lehmer, B., Tremmel, M., et al. 2013a, ApJ, 764, 41

Gladstone, J. C., Roberts, T. P., & Done, C. 2009, MNRAS, 397, 1836

Graham, J. R., Wright, G. S., Meikle, W. P. S., Joseph, R. D., & Bode, M. F. 1984, Natur, 310, 213

Harrison, F. A., Craig, W. W., Christensen, F. E., et al. 2013, ApJ, 770, 103

Heckman, T. M., Lehnert, M. D., Strickland, D. K., & Armus, L. 2000, ApJS, 129, 493

Jarrett, T. H., Chester, T., Cutri, R., Schneider, S. E., & Huchra, J. P. 2003, AJ, 125, 525

Jenkins, L. P., Roberts, T. P., Ward, M. J., & Zezas, A. 2004, MNRAS, 352, 1335

Kaaret, P. 2014, MNRAS, 440, L26

Karim, A., Schinnerer, E., Martínez-Sansigre, A., et al. 2011, ApJ, 730, 61

Kinney, A. L., Bohlin, R. C., Calzetti, D., Panagia, N., & Wyse, R. F. G. 1993, ApJS, 86, 5

Kroupa, P. 2001, MNRAS, 322, 231

Lehmer, B. D., Alexander, D. M., Bauer, F. E., et al. 2010, ApJ, 724, 559

Lehmer, B. D., Brandt, W. N., Alexander, D. M., et al. 2008, ApJ, 681, 1163

Lehmer, B. D., Wik, D. R., Hornschemeier, A. E., et al. 2013, ApJ, 771, 134

Lípari, S., Díaz, R., Taniguchi, Y., et al. 2000, AJ, 120, 645

Lira, P., Ward, M., Zezas, A., Alonso-Herrero, A., & Ueno, S. 2002, MNRAS, 330, 259

Magdziarz, P., & Zdziarski, A. A. 1995, MNRAS, 273, 837

Mapelli, M., Colpi, M., & Zampieri, L. 2009, MNRAS, 395, L71

Meurer, G. R. 2000, Massive Stellar Clusters, Vol. 211, ed. A. Lançon, & C. Boily (San Francisco, CA: ASP), 81

Miller, J. M., Parker, M. L., Fuerst, F., et al. 2013, ApJL, 775, L45

Mineo, S., Gilfanov, M., & Sunyaev, R. 2012a, MNRAS, 419, 2095

Mineo, S., Gilfanov, M., & Sunyaev, R. 2012b, MNRAS, 426, 1870

Miralles-Caballero, D., Díaz, A. I., Rosales-Ortega, F. F., Pérez-Montero, E., & Sánchez, S. F. 2014, MNRAS, 440, 2265

Mitsuda, K., Inoue, H., Koyama, K., et al. 1984, PASJ, 36, 741

Moorwood, A. F. M., & Oliva, E. 1994, ApJ, 429, 602

Moran, E. C., Lehnert, M. D., & Helfand, D. J. 1999, ApJ, 526, 649

Murphy, K. D., & Yaqoob, T. 2009, MNRAS, 397, 1549

Neff, S. G., Ulvestad, J. S., & Campion, S. D. 2003, ApJ, 599, 1043

Norris, R. P., & Forbes, D. A. 1995, ApJ, 446, 594

Pastorini, G., Marconi, A., Capetti, A., et al. 2007, A&A, 469, 405

Pastoriza, M. G., Dottori, H. A., Terlevich, E., Terlevich, R., & Diaz, A. I. 1993, MNRAS, 260, 177

Pereira-Santaella, M., Alonso-Herrero, A., Santos-Lleo, M., et al. 2011, A&A, 535, A93

Persic, M., & Rephaeli, Y. 2002, A&A, 382, 843

Pietsch, W., Roberts, T. P., Sako, M., et al. 2001, A&A, 365, L174

Prestwich, A. H., Tsantaki, M., Zezas, A., et al. 2013, ApJ, 769, 92

Rana, V., Harrison, F. A., Bachetti, M., et al. 2014, arXiv:1401.4637

Ranalli, P., Comastri, A., Origlia, L., & Maiolino, R. 2008, MNRAS, 386, 1464

Remillard, R. A., & McClintock, J. E. 2006, ARA&A, 44, 49

Sakamoto, K., Aalto, S., Combes, F., Evans, A., & Peck, A. 2014, arXiv:1403.7117

Sakamoto, K., Ho, P. T. P., & Peck, A. B. 2006, ApJ, 644, 862

Sanders, D. B., Mazzarella, J. M., Kim, D.-C., Surace, J. A., & Soifer, B. T. 2003, AJ, 126, 1607

Shakura, N. I., & Sunyaev, R. A. 1973, A&A, 24, 337

Smith, B. J., Swartz, D. A., Miller, O., et al. 2012, AJ, 143, 144

Smith, R. K., Brickhouse, N. S., Liedahl, D. A., & Raymond, J. C. 2001, ApJL, 556, L91

Soria, R., Kuntz, K. D., Winkler, P. F., et al. 2012, ApJ, 750, 152

Strickland, D. K., & Heckman, T. M. 2007, ApJ, 658, 258

Strickland, D. K., & Heckman, T. M. 2009, ApJ, 697, 2030

Strickland, D. K., Heckman, T. M., Weaver, K. A., & Dahlem, M. 2000, AJ, 120, 2965

Trancho, G., Bastian, N., Miller, B. W., & Schweizer, F. 2007, ApJ, 664, 284

Tzanavaris, P., & Georgantopoulos, I. 2007, A&A, 468, 129

Walton, D. J., Fuerst, F., Harrison, F., et al. 2013, ApJ, 779, 148

Walton, D. J., Harrison, F. A., Grefenstette, B. W., et al. 2014, arXiv:1402.2992

Wehner, E. H., Gallagher, J. S., Papaderos, P., Fritze-von Alvensleben, U., & Westfall, K. B. 2006, MNRAS, 371, 1047

Wik, D. R., Hornstrup, A., Molendi, S., et al. 2014b, ApJ, 792, 48

Wik, D. R., Lehmer, B. D., Hornschemeier, A. E., et al. 2014a, ApJ, 797, 79

Wik, D. R., Lehmer, B. D., Hornschemeier, A. E., et al. 2014b, arXiv:1411.1089

Younes, G., Porquet, D., Sabra, B., & Reeves, J. N. 2011, A&A, 530, A149

Zaritsky, D., Kennicutt, R. C., Jr., & Huchra, J. P. 1994, ApJ, 420, 87

Zenner, S., & Lenzen, R. 1993, A&AS, 101, 363